Dosed carbon precipitation and graphene layer number control on nickel micro-electromechanical systems surfaces

Gkouzou, A.; Janssen, G. C.A.M.; van Spengen, W. M.

DOI
10.1016/j.sna.2020.111837

Publication date
2020

Document Version
Final published version

Published in
Sensors and Actuators, A: Physical

Sensors and Actuators A 303 (2020) 111837

Contents lists available at ScienceDirect

Sensors and Actuators A: Physical

journal homepage: www.elsevier.com/locate/sna

Dosed carbon precipitation and graphene layer number control on nickel micro-electromechanical systems surfaces

A. Gkouzou[a,b,*], G.C.A.M. Janssen[a], W.M. van Spengen[a,c]

[a] Department of Precision and Microsystems Engineering, Delft University of Technology, 2628 CD, Delft, The Netherlands
[b] ASML Netherlands BV, De Run 6501, 5504 DR, Veldhoven, The Netherlands
[c] Falco Systems BV, Remisestraat 1, 2225 TH, Katwijk aan Zee, The Netherlands

ARTICLE INFO

Article history:
Received 3 November 2019
Received in revised form 7 January 2020
Accepted 8 January 2020
Available online 23 January 2020

Keywords:
Graphene
Chemical vapor deposition
Carbon precipitation
MEMS
Thermal time response
Micro-Raman spectroscopy

ABSTRACT

In this paper, we report on the *in situ* synthesis of graphene layers by means of chemical vapor deposition (CVD), directly on nickel micro-electromechanical systems (MEMS) surfaces. We have developed MEMS structures of which the temperature can be increased locally by Joule heating while in a methane environment. For our MEMS structures, the thermal time constant is 28 μs. As a result, we have control over the carbon precipitation time, thereby governing how many graphene layers are formed. Bi-layer to multi-layer graphene was observed using micro-Raman spectroscopy, but not single-layer graphene, as it gives no Raman signal when coupled on a nickel surface. The corresponding precipitation control theory is also presented in this paper, in which we relate the out-diffusion of carbon atoms from the grains of the nickel structure to the resulting number of graphene layers. Our method provides regulated carbon segregation from nickel and allows a prescribed number of graphene layers to form by tuning the precipitation time. In this way, we enable the direct *in situ* synthesis of graphene locally on the top and sidewalls of nickel MEMS structures, so that e.g. such graphene-coated MEMS surfaces can contribute towards a promising solution against friction and wear for MEMS devices with sliding components.

1. Introduction

Micro-electromechanical systems (MEMS) are microscopic structures with a mechanical functionality made in integrated circuit manufacturing technology, and they are found in many applications [1]. However, sliding and rotating elements are still not possible in state-of-the-art MEMS technology, because they are prone to failure due to adhesion, friction and wear [2]. In addition to avoiding sliding surfaces altogether, as the industry is now doing, new materials and techniques should be investigated to reduce friction and wear in MEMS to make such functionality possible in the future.

To lower the high friction coefficients found between the dry sliding surfaces of the commonly used MEMS materials, several lubricants have been successfully applied. While most approaches have shown potential in laboratory tests, implementing lubrication schemes in real MEMS devices with complicated structures and functions requires further research in many directions. Rymuza *et al.* deposited carbon-containing ultrathin films of silicon dioxide or silicon (oxy)nitride on silicon and metal substrates [3,4]. Carbon nanomaterials in particular, such as graphene, graphene oxide, and graphite, have received attention for their confirmed friction and wear performance both at the macroscale and the nanoscale [5]. Several studies have demonstrated that graphene has the potential to lower friction, both as single-layer [6–8], and as few-layer [9,10]. Dienwiebel *et al.* point out that the incommensurate sliding contact between a graphene flake and a graphite surface even exhibits superlubricity [11]. The use of graphene seems to be not only advantageous to 'basic' sliding MEMS structures, but also as a novel biomaterial for microscopic applications, such as nanorobots [12].

Graphene can be produced by various methods. For MEMS applications, the chemical vapor deposition (CVD) method is, in many cases, the optimum production technology, since the CVD-grown graphene forms good quality layers on a large scale, with the potential to even cover a full wafer with graphene [13]. During the CVD process, a hydrocarbon gas decomposes to carbon radicals and atoms at the catalytic surface of a metal substrate to form single- to few-layer graphene. The carbon solubility of the metal substrate determines the graphene deposition mechanism [14]. The growth mechanism of graphene on copper is self-limiting and provides the

* Corresponding author at: Department of Precision and Microsystems Engineering, Delft University of Technology, 2628 CD, Delft, The Netherlands.
E-mail address: a.gkouzou@tudelft.nl (A. Gkouzou).

https://doi.org/10.1016/j.sna.2020.111837

possibility to deposit single-layer graphene, while multiple layers can be grown on nickel [15].

Kim *et al.* have explored the deposition of graphene with the CVD process for lubrication purposes [13]. In their approach, graphene was synthesized on nickel and copper substrates, and it was transferred onto silica/silicon substrates for the subsequent tribological tests. Given the size and fragility of MEMS devices, an optimal solution should avoid the transfer step and to directly synthesize graphene on the MEMS surfaces.

Multiple papers deal with the *in situ* synthesis of graphene by CVD on nickel substrates – for a recent example, see [16] – but very few of them discuss the incorporation of graphene layers into the MEMS fabrication process flow. Zhou and Lin developed a miniature silicon platform, which was coated on top with a thin film of nickel [17]. Yu *et al.* report that a high cooling rate suppresses the amount of precipitated carbon, and that this influences the number of graphene layers that are formed [18]. Indeed, Zhou and Lin were able to deposit graphene with their system owing to a thermal time constant of about 1.3 ms. However, since they cooled directly from the in-diffusion temperature to room temperature, they had no control to the carbon precipitation time, and hence the number of graphene layers. Rybin *et al.* have demonstrate that there is a relation between the temperature-dependent electrical resistance of their nickel foils and the number of synthesized graphene layers [19]. In a recent work of Hu *et al.*, the cooling to a slightly lower temperature divides the CVD process into two stages: carbon in-diffusion and graphene growth [20].

In the work we report on here, the thermal time constant of our resistively-heated nickel MEMS structures is so small that we have control over the precipitation time, and hence the number of carbon layers that are synthesized on the surface. Furthermore, we present the theory on carbon precipitation control, and we compare it to experimental results obtained from the synthesis of graphene on nickel MEMS structures for different precipitation times.

2. Background

2.1. In-diffusion and precipitation of carbon in nickel

The graphene synthesis on nickel structures starts with the adsorption and decomposition of a hydrocarbon gas, such as methane, at the surface of the metal. The decomposition of methane takes place at temperatures above 975 K. The products of this reaction are carbon radicals, hydrogen and carbon atoms. Because of the high carbon solubility in nickel, the carbon atoms diffuse into the metal to form a nickel-carbon solid solution. The amount of carbon atoms dissolved in this solution is calculated from an Arrhenius equation that describes the dependence of carbon solubility on temperature, according to Eq. 1 [21]:

$$S = S_0 \exp\left(\frac{-H}{k_B T}\right), \tag{1}$$

where the pre-exponential factor $S_0 = 5.33 \times 10^{28}$ atomsm^{-3} is the carbon concentration in nickel at infinite temperature, $H = 6.73 \times 10^{-20}$ J is the solution energy of carbon in nickel, and k_B is the Boltzmann's constant equal to 1.38×10^{-23} JK^{-1}. Eq. 1 defines the equilibrium concentration of dissolved carbon atoms inside the nickel structure at a given temperature. Consequently, when cooled to a slightly lower temperature, the solid solution will have a carbon concentration above the saturation point; thus, the solution is supersaturated. Supersaturation of carbon in nickel-carbon solutions creates a driving force for carbon atoms to segregate from the bulk of nickel via an out-diffusion process that follows the Arrhenius law in Eq. 2 [21]:

$$D = D_0 \exp\left(\frac{-E_D}{k_B T}\right), \tag{2}$$

where the pre-exponential factor $D_0 = 2.48 \times 10^{-4}$m^{2}s^{-1} is the diffusion coefficient at infinite temperature, and E_D is the diffusion activation energy equal to 2.79×10^{-19} J. The concentration difference between the saturated and the supersaturated solution with carbon, or alternatively the carbon solubility difference between the in-diffusion and the precipitation temperature, corresponds to the amount of excess carbon atoms that will form graphene layers.

Will all the excess carbon atoms precipitate on the surface of nickel? To answer this question, we need to know how fast the out-diffusion process is, and how it depends to the geometrical dimensions of the system. In particular, the central part of our MEMS structure is a nickel beam with width w, height h, and length L. We model this beam to consist of hexagonal columnar grains with a height equal to the beam height and a diameter equal to the grain size, 2α. We assume that the grain boundaries are freeways for carbon transport, hence as soon as a carbon atom reaches a grain boundary, it will precipitate on the nickel surface. All carbon atoms within the diffusion length λ to a grain boundary or to the surface will precipitate out from the beam. The diffusion length λ of the carbon atoms inside a single grain is according to Eq. 3 [22]:

$$\lambda = 2\sqrt{D t_{\text{precipitation}}}, \tag{3}$$

where $t_{\text{precipitation}}$ is the precipitation time, and D is the diffusion coefficient calculated from Eq. 2 at the precipitation temperature. The atoms that are closest to the nickel surface are the first ones to precipitate out from the beam, and they are arranged in a hexagonal lattice to form the first graphene layer. Ideally, the precipitation of the next network of carbon atoms takes place below the first layer to form the second graphene layer, and so forth.

In reality, however, due to the grain structure of nickel, the result is not regular, and we can only make statements about the average number of layers. The hexagonal grains have a top and bottom area A, with

$$A = \frac{3}{2}\alpha^2\sqrt{3}. \tag{4}$$

The total grain boundary area equals $2whL/\alpha\sqrt{3}$ for $L >> \alpha$. All carbon that is closer to a grain boundary or to the surface than λ will reach the surface. Therefore, the volume V_C that contributes to the carbon segregation is given by:

$$V_C = 2wL\lambda + 2hL\lambda + \frac{4whL}{\alpha\sqrt{3}}\lambda. \tag{5}$$

From Eq. 6 we obtain N_C, i.e. the number of carbon atoms that will precipitate on the nickel surface:

$$N_C = V_C \Delta S, \tag{6}$$

where ΔS is the amount of excess carbon atoms due to the solubility difference between the in-diffusion and precipitation temperature. We divide N_C by the total surface area of the beam, $2(w+h)L$, to arrive at the carbon atom density on the surface, n_C. To obtain the average number of graphene layers formed by carbon precipitation, we divide the carbon atom density on the surface by the atomic density of carbon in single-layer graphene, n_{graphene} that is equal to 3.8×10^{19} atomsm^{-2} [23], hence $n = n_C/n_{\text{graphene}}$. Eq. 7 is the relation between the average number of graphene layers that are formed, and the amount of excess carbon atoms due to the solubility difference between the in-diffusion and precipitation temperature:

$$\frac{n}{\Delta S} = \frac{w + h + \frac{2wh}{a\sqrt{3}}}{(w+h)n_{\text{graphene}}}\lambda. \tag{7}$$

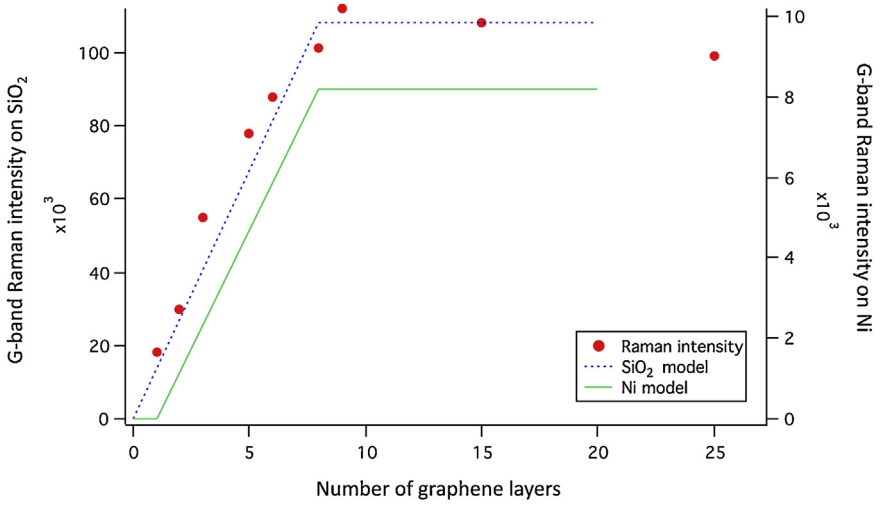

Fig. 1. G-band Raman intensity as a function of number of graphene layers. Experimental data adapted from [25], with the proposed first order intensity model for the Raman response of graphene on nickel.

The largest value for $n/\Delta S$ is obtained in the situation where the whole volume has been emptied of excess carbon atoms. This happens when $V_C = whL$, and Eq. 5 is reconstructed according to:

$$\lambda = \frac{wh}{2\left(w + h + \frac{2hw}{\alpha\sqrt{3}}\right)} . \tag{8}$$

Longer diffusion lengths λ will have no influence on the number of graphene layers that are grown.

2.2. Raman spectroscopy for graphene layer number identification

To assess the number of graphene layers that are synthesized by the CVD process, and how these layers are spatially distributed over the surface topography of the nickel structures, we used micro-Raman spectroscopy. It is a standard technique used to observe molecular vibrations, phonons, and other excitations in a crystal lattice, which correspond to certain frequencies; thus, this method provides valuable information about the material of interest, and, in our case, it can help us in determining the number of graphene layers.

For free-standing graphene, or graphene on a weakly interacting surface such as SiO_2, two Raman peaks appear at wavenumbers of ~ 1580 cm^{-1} and ~ 2700 cm^{-1}; these peaks correspond to the G-band and the 2D-band, respectively [24]. For single-layer graphene, the 2D-band has a much higher intensity than the G-band. For bi-layer graphene, the two bands have approximately the same intensities. For few-layer graphene, the intensity of the G-band is much higher than the one of the 2D-band, and the intensity ratio increases with increasing number of layers. An important aspect of micro-Raman spectroscopy on graphene is the very strong Raman signal emanating from few-layer graphene. The Raman intensity of single-layer graphene is almost as high as the Raman intensity of bulk (pyrolytic) graphite [25]. For the first nine layers, the intensity increases more or less linearly, after which it starts decreasing until it reaches the intensity of bulk graphite.

Unfortunately, nickel has a surface that strongly interacts with graphene. As a consequence, single-layer graphene on nickel does not normally give a Raman signal, unless the film is loose or stretched [26]. Indeed, in the Raman spectra obtained for this paper, no single-layer graphene is observed, as will be shown later. Note that most papers detailing micro-Raman spectroscopy of single-layer graphene films grown on nickel present Raman data of the film after it has been transferred to SiO_2. There is no data available in literature on the Raman intensity as a function of the number of graphene layers of graphene coupled on nickel. Therefore, we assume that from the second layer onward, graphene will mainly interact with itself, instead of with the nickel surface underneath. As a result, the synthesized graphene layers are expected to show G-band Raman intensity as a function of layer thickness relation similar to the measured data shown in Fig. 1, only this time shifted by one layer. We can then assume that the G-band Raman intensity observed is linear to the number of layers, with zero intensity corresponding to one layer or less. This is a reasonable approximation, as long as the layer thickness is in between 1 and 8 layers. As we expect to grow no more than ~ 20 layers in our experiments, we can assume that the G-band Raman intensity becomes essentially constant above 8 layers. As the maximum precipitation time is so long that all excess carbon precipitates out of the nickel beam, we can use the spectrum with the highest observed G-band Raman intensity (to be discussed in Section 5.1) to calibrate the number of layers for the other intensities. With the highest intensity obtained in our experiments being 8200 (a.u.), the scale for the G-band Raman intensity on nickel as a function of number of graphene layers can be added to Fig. 1 on the right-hand side.

It is important to mention the possibility to observe one more band in the graphene Raman response. This regards the D-band, which appears at ~ 1350 cm^{-1}. This peak is evidence of structural defects that are usually present in CVD-grown graphene. The D-band appears in several Raman spectra when probing locations covered with single-layer graphene. This peak disappears with increasing number of layers: The more carbon precipitates on the surface, the higher the probability becomes for additional atoms to fill up the empty sites of the hexagonal lattice.

Since it is the precipitation time that governs the number of graphene layers in our deposition experiments, we expect to get a Raman response per precipitation time similar to the ones plotted in Fig. 2, except for the missing single-layer graphene response. The Raman response is the footprint of the graphene layer number, which we control through tuning of the precipitation time. A long precipitation time will resemble the Raman response of few-layer graphene, while a faster precipitation time will give the Raman signal of bi-layer, and not single-layer, graphene. Meanwhile, for very short precipitation times, we will observe only the background noise of the Raman measurement since no graphene layers will be formed on the nickel surfaces.

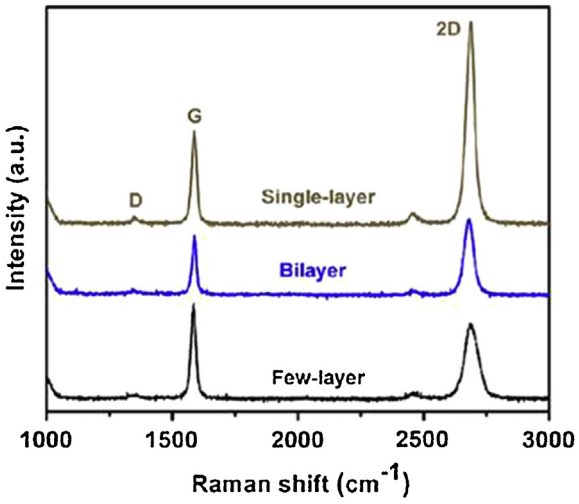

Fig. 2. Raman response of single-layer, bi-layer and few-layer graphene (reprinted from [27] with permission from Elsevier®).

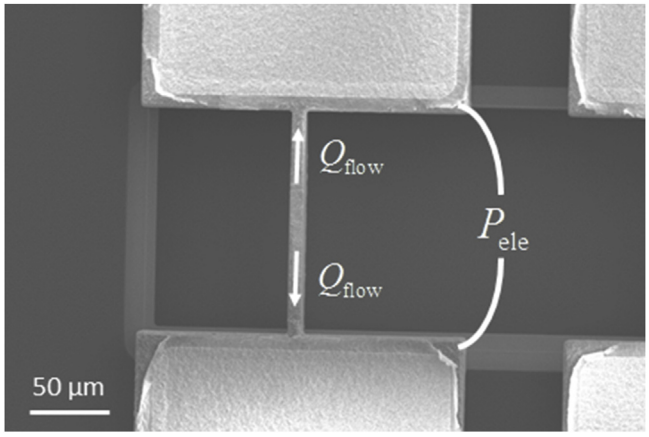

Fig. 3. SEM micrograph of the MEMS structure with an 8-μm wide beam.

3. Experimental details

3.1. The MEMS structures

The MEMS structures were fabricated in a micromachining process by MEMSCAP Inc., known as MetalMUMPs™, which uses a 20-μm thick electroplated nickel layer [28]. The structures are 80-μm long free-standing beams that are either 8-μm or 6-μm wide. Thus, the volume of an 8-μm wide beam is $12.8 \times 10^3 \mu m^3$, while the volume of a 6-μm wide beam is $0.96 \times 10^3 \mu m^3$. The nickel structures are clamped by bondpads and suspended over a 25-μm deep trench. The suspension ensures that there are no conductive heat losses through the silicon substrate below. A scanning electron micrograph of the MEMS structure with an 8-μm wide beam is shown in Fig. 3.

Electrical drive signals are applied to the bondpads of the MEMS structure in order to induce Joule heating of the beam. For a beam length of 80 μm, the thermal time constant is 28 μs (see Appendix for analytical model to obtain this number).

3.2. Raman setup

The Raman spectra were obtained on a HORIBA Scientific LabRam HR micro-Raman spectrometer with excitation from an argon-ion laser with a 514-nm wavelength, and a 50× objective lens with a numerical aperture of 0.5. This results in a spatial resolution of around 1.25 μm.

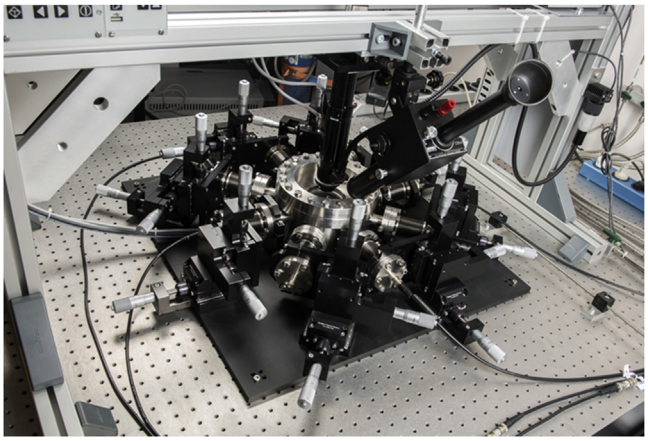

Fig. 4. Photo of the vacuum probe system. A turbomolecular pump is connected to the chamber via a hole in the middle of the vibration isolation table, so it is not visible in this figure.

Table 1
The impurities of Linde Hydrogen 5.0 detector gas and Linde Methane 5.5 scientific gas.

Hydrogen 5.0 detector		Methane 5.5 scientific	
≥ 99.999 vol%	H_2	≥ 99.9995 vol%	CH_4
≤ 3 vpm	N_2	≤ 5 vpm	O_2+N_2
≤ 5 vpm	H_2O	≤ 1 vpm	C_xH_y
≤ 2 vpm	O_2	≤ 1 vpm	H_2O
≤ 0.5 vpm	C_xH_y		

3.3. The vacuum probe system

For the local heating of the MEMS structures, a customized micro-manipulator probe system was purchased from McAllister Technical Services. Our MEMS structures are fabricated on a wafer that is diced into 5-mm-square semiconductor chips that can be placed inside the chamber of the probe system. The user has optical access to the chip through a viewport on the top of the chamber. The probe system is mounted on a vibration isolation table with a hole in the middle via which the chamber is connected to a pumping system. Prior to the deposition experiments, a roughing pump produces a pressure of 10^{-3} mbar, which is low enough for a turbomolecular pump to achieve a base pressure of the order of 10^{-8} mbar. The chamber is then isolated from the pump via a gate valve, and it is filled with either hydrogen or methane through gas lines. Fig. 4 shows the vacuum probe system, and Table 1 lists the impurities of the hydrogen and methane gases supplied by Linde Gas Nederland.

3.4. Four-point measurement setup

For the Joule heating of the nickel MEMS structures, the electrical drive signals are supplied by a data acquisition device (National Instruments, NI USB X Series Multifunction DAQ) that is connected to a computer. The two bondpads of the MEMS structure are connected by probes to analog output and ground, respectively. With two additional probes on the same bondpads, we measure the voltage across the structure by a voltmeter. A high-current 1× buffer amplifier has been developed in-house and has been included in the circuit to compensate for the different impedance levels between the output of the DAQ device and the input of the MEMS structure. Moreover, we have added a 10-Ohm power resistor to ensure

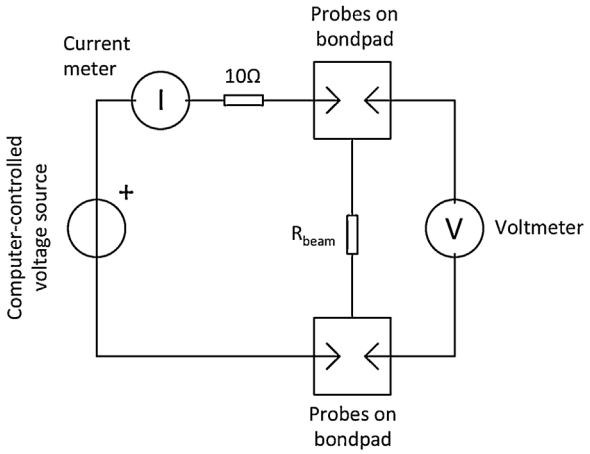

Fig. 5. Electrical wiring diagram of the four-point measurement setup. The circuit allows setting of the temperatures in the graphene synthesis experiments.

that the current flowing through the beam is not defined by the probe/bondpad contact resistance, or by any other varying or parasitic resistance in the circuit. Fig. 5 shows the electrical wiring diagram of the four-point measurement setup. Through this circuit, we are able to control the electrical power that is dissipated due to the voltage drop across the structure, which we can relate to the temperature increase necessary to deposit graphene locally, in the middle part of the beam.

3.5. Procedure and test conditions

The electrical resistance of the beams increases with the increase in temperature, which leads to a higher than intended voltage across the structure. The voltage values can differ from beam to beam, even if the same drive signal is supplied by the DAQ device. Therefore, we established a procedure to prevent the beam from overheating: The experiments are performed in a number of steps, and, during each step, we increase the value of the set drive signal with the square root of time. At the end of every step, we inspect the beam with micro-Raman spectroscopy, and assess whether and how many graphene layers have formed. In the subsequent step, we take a slightly higher final value for the drive signal.

To start the deposition experiments, we first place the chip with the structure inside the chamber that is then pumped down to vacuum. We flush the chamber with hydrogen, and we set a low drive signal to induce Joule heating of the structure. In this way, we carry out a low-temperature treatment using hydrogen annealing before the CVD process. During the annealing stage, we measure both the voltage and the current across the MEMS structure. To convert measured electrical power to annealing temperature, we use the expression we derived from our FEM model (see Appendix).

Afterwards, we pump out the hydrogen and introduce methane in the chamber. For the in-diffusion stage, we set the same drive signal as the one for the annealing stage, whereas the drive signal is set lower by 0.5 V for the precipitation stage. We observe that the measured voltage is now slightly higher compared to the one when the structure was in a hydrogen environment, indicating that, during the in-diffusion stage, the increasing content of dissolved carbon atoms increases the electrical resistance of the beam. Therefore, for this structure and for the same drive signal, the in-diffusion temperature is higher than the annealing temperature. We convert measured power to in-diffusion or precipitation temperature by using the same expression derived from FEM modeling, since it holds for any surrounding atmosphere.

The chamber is subsequently vented, so that we can remove the chip and examine the top surface of the beam for graphene growth with micro-Raman spectroscopy. Because the in-diffusion temperature is still too low, no layers are present on the surfaces of the nickel beam. We then place the chip back inside the chamber, which we first evacuate and then repeat the experimental procedure. In this next step of experiments, we set a slightly higher drive signal for the annealing/in-diffusion stage, while, for the precipitation stage, the drive signal is again set lower by 0.5 V. A couple more steps of experiments follow until the Raman response indicative of graphene layers is acquired.

In all experiments, the chamber pressure is 1000 mbar, and both the annealing and in-diffusion times are 120 s. The precipitation times were set to 0.5 μs, 0.01 s, and 30 s, and are expected to yield nothing, few-, and multi-layer graphene, respectively. As the thermal time constant of the MEMS device is 28 μs (see Appendix), we will use this value to indicate the shortest precipitation time. Note that while at the 0.01-s and 30-s precipitation times the cooling occurs effectively instantaneously compared to the total time, the 28-μs precipitation time has an exponentially decreasing cooling profile. At the end of every stage, the electrical drive signal is set to zero, and the time required for the structure to cool down to room temperature is defined by its thermal time constant. We have observed that, at constant current, the output voltage decreases by a few percent due to a change in electrical resistance across the beam, with a time constant in the order of seconds. We refer to this effect as voltage sag, and it translates to a temperature decrease that causes undesirable carbon precipitation during the in-diffusion stage. To prevent this, instead of setting the DC input voltage instantly, we ramp the drive signal with the square root of time for 120 s. During this time, the temperature of the structure increases with the square root of time till it reaches its maximum value that relates to the set drive signal. The diffusion of carbon into nickel happens predominantly in the last ten seconds of this stage. We hence use the 'effective in-diffusion temperature', which is the temperature defined as being halfway between the in-diffusion temperature and the precipitation temperature, so that we can estimate the amount of excess carbon concentration. We ramp the drive signal during the in-diffusion, as well as the annealing stage. Fig. 6 summarizes the conditions under which the graphene deposition experiments are carried out. In this figure, the duration of the precipitation stage is 30 s.

4. Results

Table 2 summarizes all the graphene deposition experiments classified in terms of precipitation time: 28 μs (with the electrical precipitation time set to 0.5 μs), 0.01 s, and 30 s. Each precipitation time was tested on two MEMS structures with an 8-μm wide beam and a 6-μm wide beam (second column). The experiments were carried out in a number of steps (first column) following the procedure described in the 'Procedure and test conditions' section of this paper. The measured electrical power values have been converted to temperature values by using the formulas derived from the FEM model (see Appendix). T_{anneal} is the temperature during the annealing stage while in hydrogen environment. T_{in} is the temperature at the end of the in-diffusion stage, and T_{prec} is the temperature during the precipitation stage while in methane environment.

In Figs. 7, 8 and 9 we plot the Raman response of all MEMS structures. They illustrate the evolution of the graphene layer growth with increasing in-diffusion and precipitation temperature for a MEMS structure with a 6-μm wide beam (left), or an 8-μm wide beam (right), for the three set precipitation times: 28 μs, 0.01 s, and 30 s. All spectra seen in these figures contain two sharp plasma lines that are indicative of the argon-ion laser transitions [29].

We carried out one more graphene deposition experiment on another MEMS structure with an 8-μm wide beam, and with a

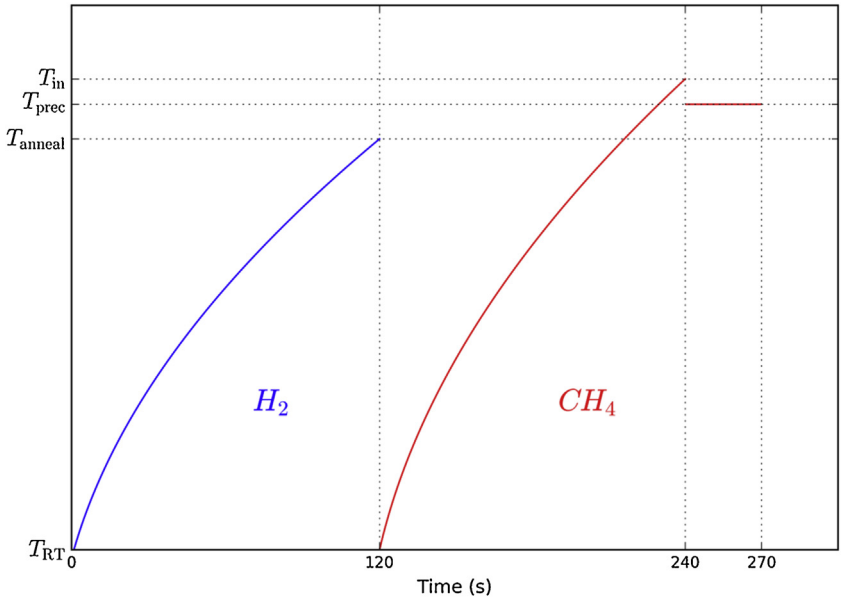

Fig. 6. Diagram of the temperature profile during the graphene deposition experiments.

Table 2
Overview of the graphene deposition experiments.

		28 μs			0.01 s			30 s		
Step number	Beam width	T_{anneal}	T_{in}	T_{prec}	T_{anneal}	T_{in}	T_{prec}	T_{anneal}	T_{in}	T_{prec}
1	6 μm	755 K	830 K	780 K	800 K	865 K	810 K	765 K	850 K	805 K
	8 μm	810 K	870 K	830 K	775 K	840 K	790 K	780 K	870 K	835 K
2	6 μm	820 K	870 K	820 K	820 K	880 K	830 K	795 K	940 K	895 K
	8 μm	790 K	915 K	875 K	815 K	865 K	835 K	835 K	870 K	835 K
3	6 μm	830 K	930 K	885 K	870 K	985 K	930 K	875 K	930 K	890 K
	8 μm	845 K	965 K	935 K	815 K	930 K	890 K	860 K	935 K	900 K
4	6 μm	870 K	995 K	950 K	950 K	970 K	915 K	895 K	1030 K	985 K
	8 μm	905 K	1000 K	975 K	910 K	980 K	955 K	895 K	990 K	960 K
5	6 μm	930 K	1025 K	975 K	900 K	1050 K	1000 K	1030 K	1120 K	1070 K
	8 μm	955 K	1040 K	1005 K	875 K	950 K	915 K	915 K	990 K	955 K

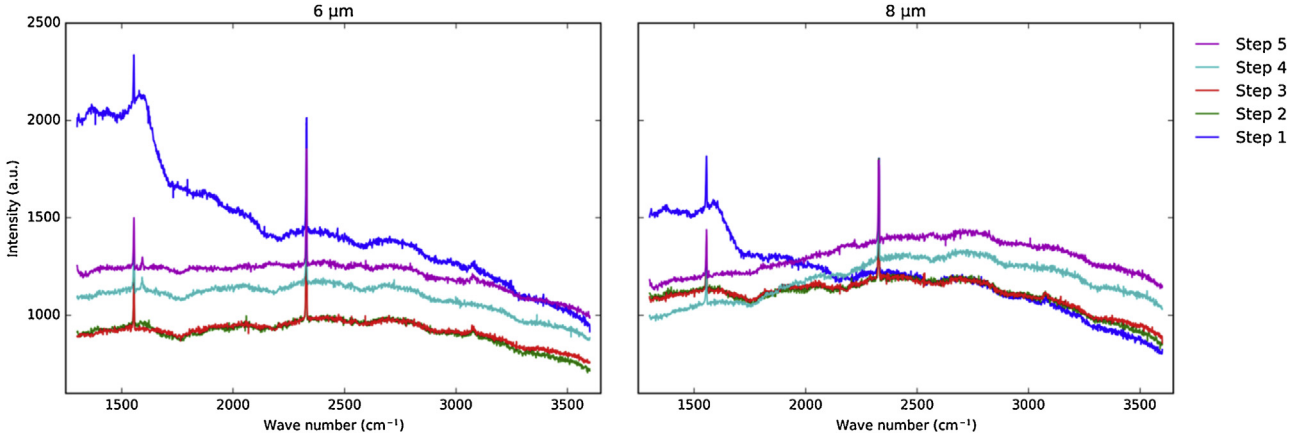

Fig. 7. Raman response of all steps of experiments with a precipitation time of 28 μs on the 6-μm wide beam (left), and on the 8-μm wide beam (right). No graphene growth is observed.

precipitation time of 0.3 s. We followed the same procedure as in the previous graphene layer growth procedure. Fig. 10 shows the Raman response at the middle part of the beam, and Fig. 11 is an image of the MEMS structure and its Raman responses at four other locations of the beam with their distance from the middle part indicated on top of each plot. Figs. 10 and 11 show the Raman response from the final step of experiments. The spread in Raman signal intensity is indicative of a difference in layer thickness from location to location. Single-layer graphene is observed nowhere on the structure, consistent with the theory that single-layer graphene is not Raman-active when coupled on a nickel surface.

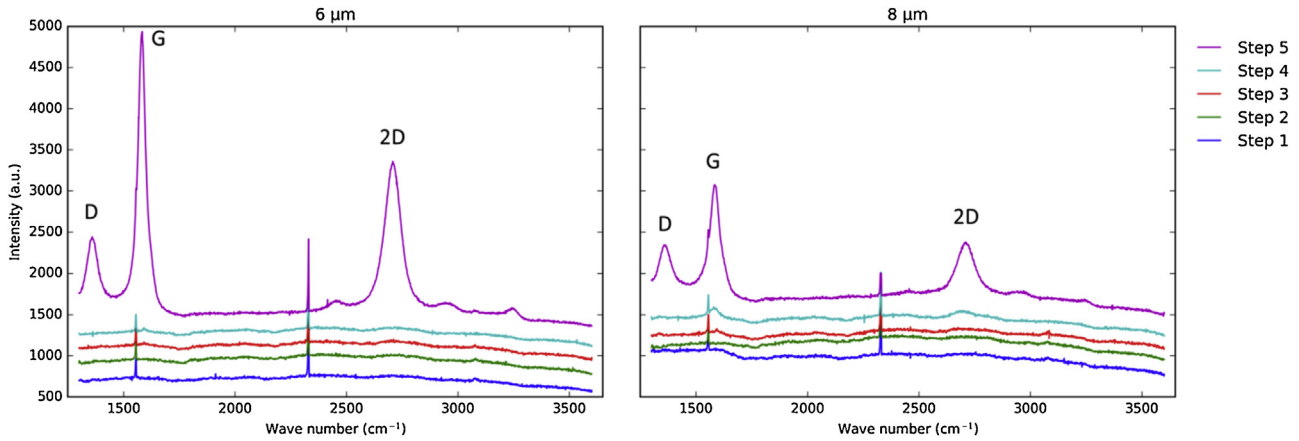

Fig. 8. Raman response of all steps of experiments with a precipitation time of 0.01 s on the 6-µm wide beam (left), and on the 8-µm wide beam (right). Few-layer graphene growth is observed.

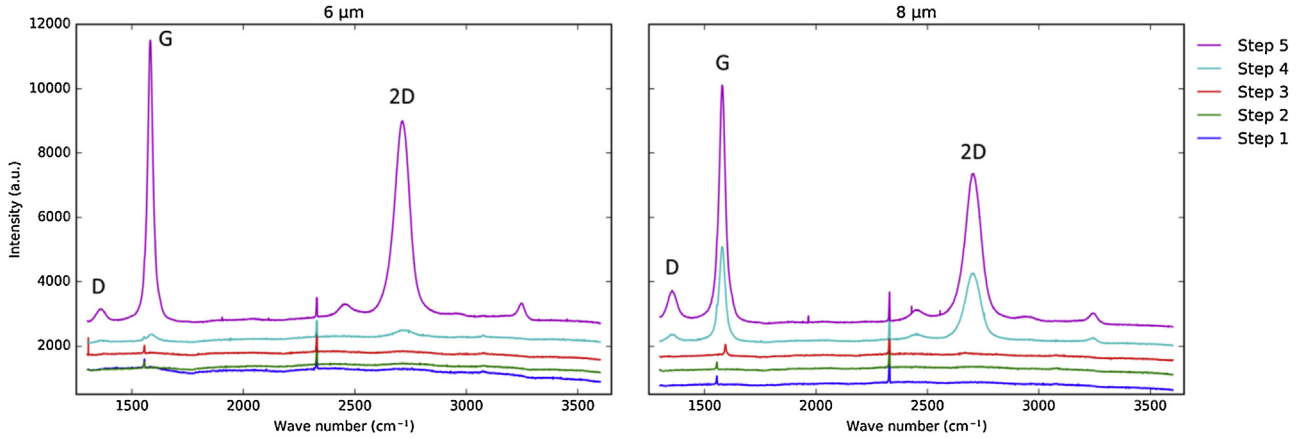

Fig. 9. Raman response of all steps of experiments with a precipitation time of 30 s on the 6-µm wide beam (left), and on the 8-µm wide beam (right). Multi-layer graphene growth is observed.

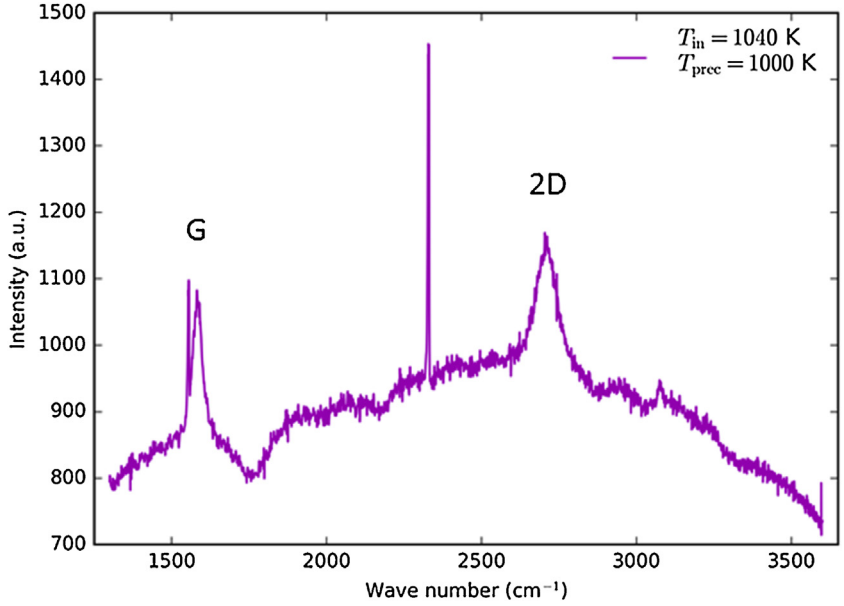

Fig. 10. Raman response of the final step of graphene deposition experiments with a precipitation time of 0.3 s on an additional MEMS structure with an 8-µm wide beam.

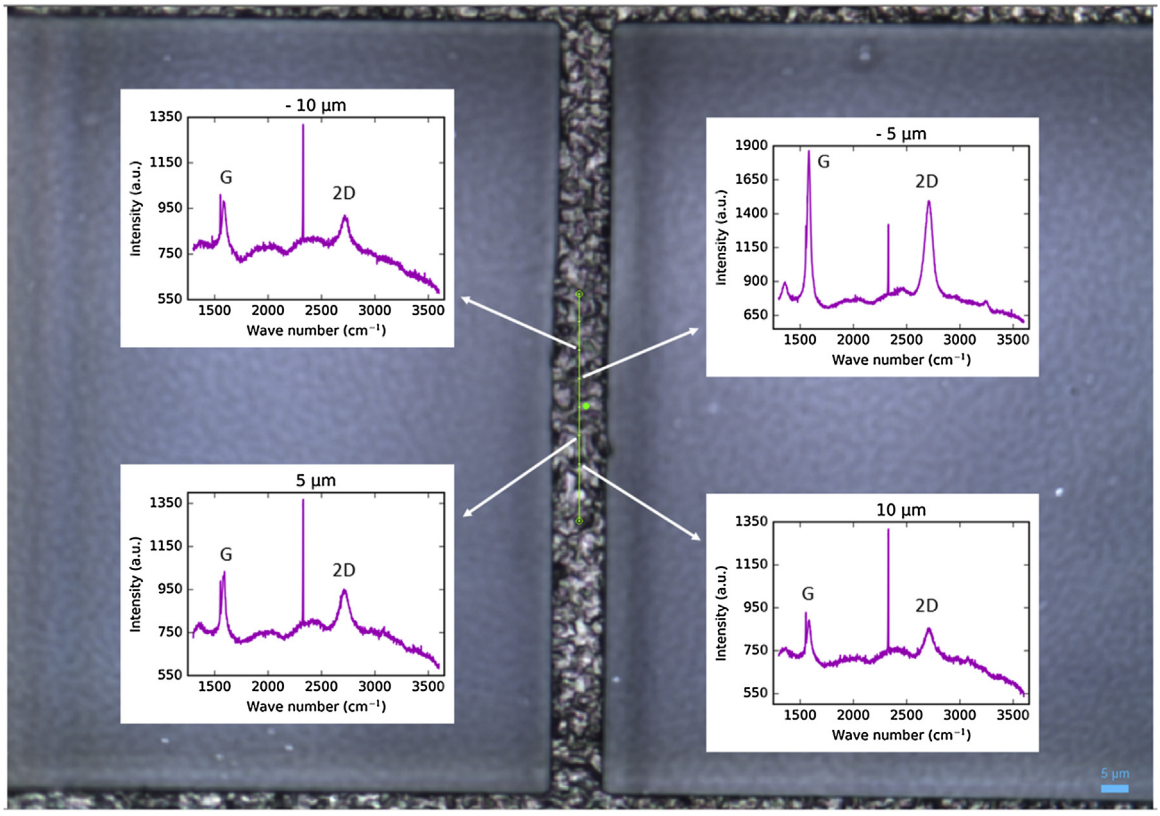

Fig. 11. Raman response of the final step of graphene deposition experiments with a precipitation time of 0.3 s at four other locations of the beam with their distance from the middle part indicated on top of each plot.

5. Discussion

5.1. Number of graphene layers deposited on the nickel MEMS surfaces

The experiments in which the duration of the precipitation stage was 30 s yielded multiple layers of graphene, so many that it is in fact more appropriate to speak of a thin graphitic film. There is a large difference between many physical properties of graphene and graphite, but for our purpose, which is the modification of tribological properties of MEMS surfaces, both are desirable. In step 5, multiple layers of graphene were formed on both structures with a 6-µm wide beam and an 8-µm wide beam, with the layer number of the former being much higher than the one of the latter due to slightly higher in-diffusion and precipitation temperature. However, in the previous step, the structure with an 8-µm wide beam indicated the formation of more graphene layers, even though both the in-diffusion and precipitation temperature were lower than the ones of the 6-µm wide beam. This is probably due to the fact that the temperature of the hydrogen annealing stage at the 6-um beam was too low to provide a 'clean' surface prior to the CVD process that took place at such high in-diffusion and precipitation temperature. Thus, although this step resulted in no layer deposition, it nevertheless contributed to the total graphene growth history of the structure. Note that when the temperature of a graphene-coated structure increases, the deposited graphene layers dissolve back in the bulk of the structure in the form of carbon atoms [30]. Moreover, in the previous step of experiments for the 8-µm wide beam, both the in-diffusion and precipitation temperatures were slightly higher compared to the ones of the 6-µm wide beam. Thus, during this step, the nuclei for the subsequent synthesized graphene layers could have been formed.

The experiments in which the duration of the precipitation stage was 0.01 s yielded few layers of graphene. In particular, for the MEMS structure with an 8-µm wide beam, the synthesis of few-layer graphene took place in step 4, since both the in-diffusion and precipitation temperatures were slightly higher than the ones measured at the middle part of the 6-µm wide beam. In step 5, the structure with a 6-µm wide beam had both the in-diffusion and precipitation temperatures higher than the ones of the 8-µm wide beam, and hence the number of graphene layers that were formed was larger. In these figures, we observe a clear D-band that is indicative of defects in the graphene lattice. The intensity of the D-band decreases with the increase in intensity of the Raman signal, meaning that the multi-layer graphene is more defect-free, as described in Section 2.2.

The experiments in which the duration of the precipitation stage was 28 µs yielded no observable Raman signal, since this time corresponded to a diffusion length that was well below the minimum distance that the carbon atoms needed to move to form even a single layer of graphene. Virtually no carbon atoms precipitated out from the bulk of the structure. Thus, in Fig. 7, we only observe the background noise of the Raman measurement, which adds weight to the claim that the graphene growth mechanism is carbon out-diffusion-limited.

In Fig. 10 and Fig. 11, we show the Raman response of the additional MEMS structure with an 8-µm wide beam, where the precipitation stage lasted 0.3 s. The deposition experiments yielded bi-layer graphene at the middle of the beam and few-layer at other locations, where both the in-diffusion and precipitation temperatures are expected to be slightly lower than the calculated ones (1040 K and 1000 K, respectively). With this MEMS structure, we show that the intensity and Raman peak ratio of the spectra varies significantly from location to location on the nickel surface (see

Table 3
Measured G-band intensity counts seen in Figs. 8–10, and their respective calculated number of graphene layers from the Raman responses that correspond to each precipitation time.

Precipitation time	G-band intensity counts		Number of graphene layers	
	6 μm	8 μm	6 μm	8 μm
28 μs	0	0	0 (<1)	0 (<1)
0.01 s	3100	1300	3–4	2
30 s	8200	7300	>8 (calculated: 16)	>8 (calculated: 8–9)

Fig. 11). Our interpretation of these data is that due to the limited spatial resolution of the micro-Raman spectroscope being 1.25 μm, we probe different patches of graphene at the same time. Some of the surface is bare nickel, some may be bi-layer graphene, and part is certainly multi-layer, given the Raman peak ratio. This means that the patches that are grown first (maybe preferentially at the grain boundaries) are smaller than 1.25 μm in diameter, and that a second layer starts to form at the nucleation sites long before the first layer is complete. With prolonged precipitation, the layer grows thicker, but presumably it is still not equally thick in all locations. Another striking finding is the fact that a multi-layer graphene Raman response is found in spectra with sub-single-layer intensity. This is indicative of the fact that single-layer graphene may exist on the surface but is not visible with Raman.

From Fig. 8 and Fig. 9, we extracted the number of graphene layers deposited at the end of every step that resulted in a Raman response. Table 3 lists the number of graphene layers for each precipitation time and beam width of the MEMS structure after step 5. The procedure for calculating the number of layers from the G-band Raman intensity on a nickel surface is described in Section 2.2. If we assume that all carbon has precipitated out in 30 s, we have a reference to which the G-band Raman intensities can be compared. The number of layers is given in brackets for the 30-s precipitation time experiment as calculated from Eq. 7, showing that we indeed reach the maximum G-band Raman intensity of Fig. 1. The meaning of a partial number of layers of graphene is that these layers are incomplete, e.g. a layer thickness of 3–4 will consist of a film that is partly three, partly four layers thick within the probing area. With micro-Raman spectroscopy, we have a spot size limiting the in-plane spatial resolution to ~ 1 μm. Hence, we cannot distinguish between a situation with many different perfect grains smaller than our resolution, and a situation with only one grain but with many defects. The fact that we see partial numbers of layers (Table 3) again indicates that also in this respect the variation takes place on a length scale that we cannot probe optically.

In Fig. 12, the Raman intensity of the G-band is shown as a function of precipitation time, while Fig. 13 presents the calculated graphene layer thickness.

5.2. *Normalized number of graphene layers as a function of diffusion length*

In Fig. 14, we plot the normalized number of graphene layers deposited on the beams as a function of the total diffusion length, according to Eq. 8. This has the advantage of resulting in a plot that is independent of the individual temperature steps encountered in the experiments. For the two experiments where the precipitation time was 28 μs, which yielded virtually no graphene, we added error bars from zero to a single, undetectable graphene layer and placed the dots at half a layer to distinguish between the 6- and 8-μm wide beams. For the remaining four MEMS structures, we plot their $\eta/\Delta S$ values using the respective number of graphene layers listed in Table 3.

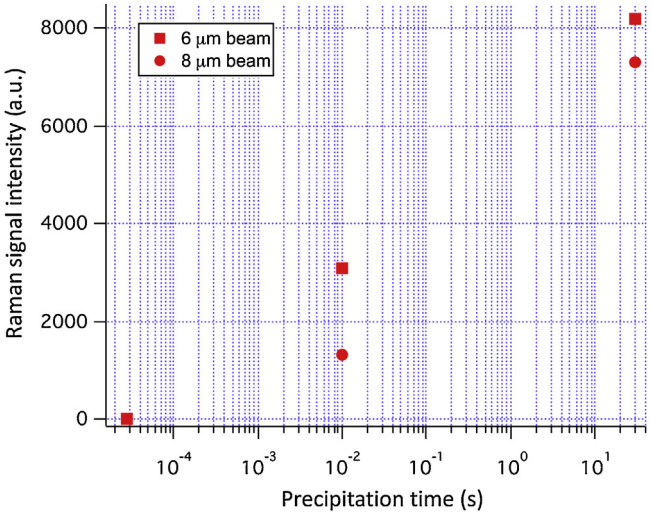

Fig. 12. Measured G-band Raman intensity as a function of precipitation time.

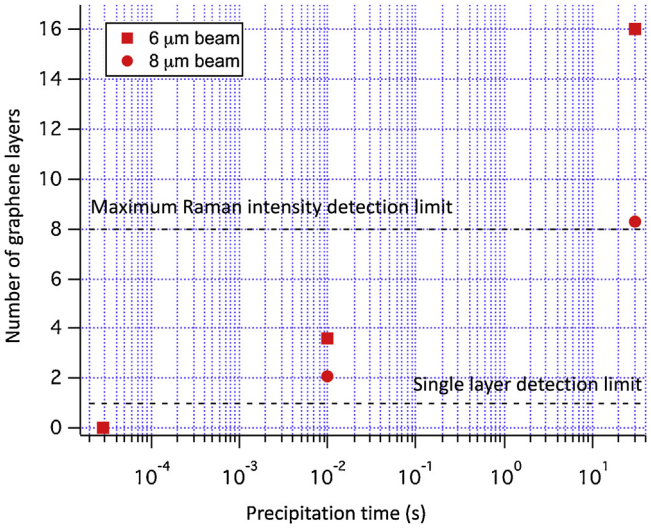

Fig. 13. Calculated number of graphene layers as a function of precipitation time.

On the y axis of Fig. 14, the normalized number of graphene layers consists of the calculated number of layers divided by its respective carbon solubility difference for each beam width, and it is proportional to the fraction of the excess carbon that precipitates on the nickel surface. On the x axis, we plot the calculated diffusion length for the measured temperatures and the corresponding precipitation time. When the diffusion length becomes longer than the maximum value calculated from Eq. 8, all the excess carbon atoms will precipitate on the surface of nickel and no more layers will be synthesized, hence the horizontal plateau in Fig. 14. Moreover, in the calculations of the total diffusion length, we set the size of the hexagonal grains equal to $2\alpha = 1$ μm. This grain size is typical for nickel structures that are fabricated using the MetalMUMPs process [31], and it fits the data plotted in Fig. 14 very well.

Overall, the number of synthesized graphene layers approximates the predicted trend in Fig. 14. The agreement is good, given that, in addition to the temperature measurement errors, there are several more effects that were not included in our theory on carbon precipitation control. For instance, the model takes for granted that carbon atoms are uniformly distributed inside the nickel structure during the in-diffusion stage, and similarly it presumes that the excess carbon atoms are homogeneously segregated from the nickel-carbon solution, hence assuming uniform distribution on the

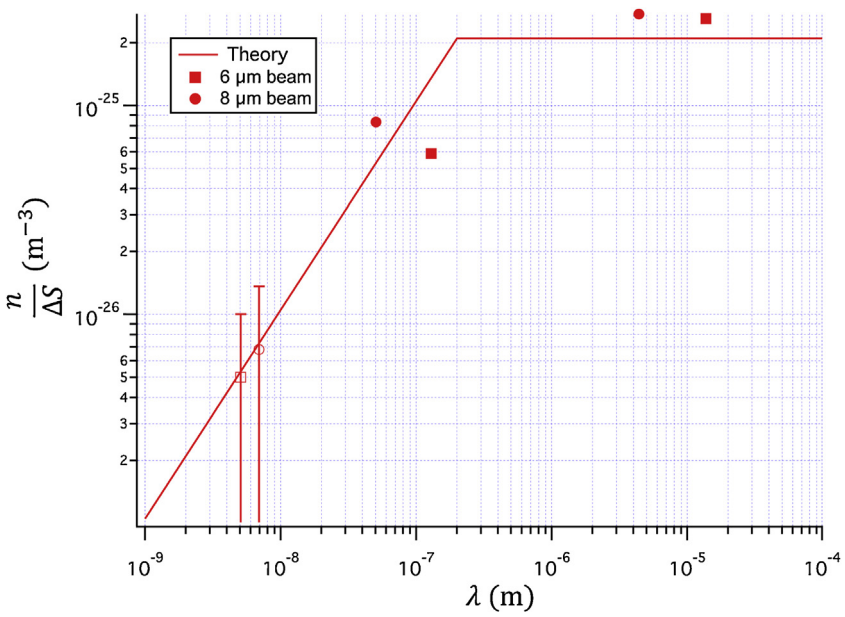

Fig. 14. The normalized number of graphene layers deposited on the beams of the MEMS structures as a function of diffusion length.

nickel surface during the precipitation process. The effects of surface roughness of the nickel structure and the effect of nucleation kinetics on the graphene growth mechanism are likewise considered negligible.

6. Conclusion and future work

In this paper, we have presented our theory on carbon precipitation control which we compared to the results from our graphene CVD experiments on nickel MEMS structures. The experiments were performed by independently controlling the temperatures during the carbon in-diffusion and precipitation stages, and their respective duration. Because the MEMS device we used has a thermal time constant of only 28 μs, we were able to precisely control the precipitation time and hence the number of carbon atoms that diffused out and precipitated on the nickel surface, which ultimately influences the number of graphene layers that were formed. We have shown that it is necessary to incorporate grain-boundary diffusion in the model to obtain agreement between the predicted number of graphene layers and the measured one. By adjusting the precipitation time, we were able to change the number of graphene layers formed from virtually zero (owing to the short thermal time constant) up to the number of layers where all dissolved carbon atoms contribute to the formed graphene layers. No monolayer graphene was observed in the Raman spectra, which is consistent with the theory that single-layer graphene on a nickel surface is not Raman-active. Our method can be used in future experiments where graphene-coated MEMS structures are needed e.g. to slide against one another in MEMS devices with a tribomechanical functionality. This may take the form of experiments with dedicated nickel MEMS tribometers, similar to the similar in functionality to the MEMS tribometers presented earlier in [32].

Authorship statement

All persons who meet authorship criteria are listed as authors, and all authors certify that they have participated sufficiently in the work to take public responsibility for the content, including participation in the concept, design, analysis, writing, or revision of the manuscript. Furthermore, each author certifies that this material or similar material has not been and will not be submitted to or published in any other publication before its appearance in *Sensors and Actuators A: Physical*.

Declaration of Competing Interest

The authors declare that they have no known competing financial interests or personal relationships that could have appeared to influence the work reported in this paper.

Acknowledgements

This work is part of the research programme 'Fundamental aspects of friction' under ref no. 129 of the NWO Institute Organisation (NWO-I), which is part of the Netherlands Organisation for Scientific Research (NWO).

Appendix A. Supplementary data

Supplementary material related to this article can be found, in the online version, at doi:https://doi.org/10.1016/j.sna.2020.111837.

References

[1] M.J. Madou, Fundamentals of Microfabrication: the Science of Miniaturization, 2nd ed., CRC Press, Boca Raton, 2002.
[2] W.M. van Spengen, MEMS reliability from a failure mechanisms perspective, Microelectron. Reliab. 43 (2003) 1049–1060.
[3] Z. Rymuza, Z. Kusznierewicz, M. Misiak, K. Schmidt-Szałowski, Z. Rżanek-Boroch, J. Sentek, in: B. Bhushan (Ed.), Wear and Nanomechanical Studies of Silicon Oxide and Silicon Nitride Thin Films for MEMS Applications, in *Tribology Issues and Opportunities in MEMS*, Springer, Dordrecht, 1998, pp. 579–589.
[4] Z. Rymuza, M. Misiak, Z. Rżanek-Boroch, K. Schmidt-Szałowski, J. Janowska, The effect of deposition and test conditions on nanomechanical behavior of ultrathin films produced by plasma-enhanced chemical vapour deposition process at atmospheric pressure, Thin Solid Films 466 (2004) 158–166.
[5] W. Zhai, N. Srikanth, L.B. Kong, K. Zhou, Carbon nanomaterials in tribology, Carbon 119 (2017) 150–171.
[6] D. Berman, S.A. Deshmukh, S.K.R.S. Sankaranarayanan, A. Erdemir, A.V. Sumant, Extraordinary macroscale wear resistance of one atom thick graphene layer, Adv. Funct. Mater. 24 (2014) 6640–6646.
[7] Q. Wang, B. Bai, Y. Li, Y. Jiang, L. Ma, N. Ren, Investigating the nanotribological properties of chemical vapor deposition-grown single layer graphene on SiO_2 substrates annealed in ambient air, RSC Adv. 5 (2015) 10058–10064.

[8] S. Kwon, J.H. Ko, K.J. Jeon, Y.H. Kim, J.Y. Park, Enhanced nanoscale friction on fluorinated graphene, Nano Lett. 12 (2012) 6043–6048.
[9] T. Filleter, J.L. McChesney, A. Bostwick, E. Rotenberg, K.V. Emtsev, T. Seyller, K. Horn, R. Bennewitz, Friction and dissipation in epitaxial graphene films, Phys. Rev. Lett. 102 (2009), 086102.
[10] M. Tripathi, F. Awaja, G. Paolicelli, R. Bartali, E. Iacob, S. Valeri, S. Ryu, S. Signetti, G. Speranza, N.M. Pungo, Tribological characteristics of few-layer graphene over Ni grain and interface boundaries, Nanoscale 8 (2016) 6646–6658.
[11] M. Dienwiebel, G.S. Verhoeven, N. Pradeep, J.W.M. Frenken, J.A. Heimberg, H.W. Zandbergen, Superlubricity of graphite, Phys. Rev. Lett. 92 (2004), 126101.
[12] A.V. Singh, P. Laux, A. Luch, S. Balkrishnan, S.P. Dakua, Bottom-UP assembly of nanorobots: extending synthetic biology to complex material design, Front. Nanosci. Nanotechnol. 5 (2019) 1–2.
[13] K.S. Kim, H.J. Lee, C. Lee, S.K. Lee, H. Jang, J.H. Ahn, J.H. Kim, H.J. Lee, Chemical vapor deposition-grown graphene: the thinnest solid lubricant, ACS Nano 5 (2011) 5107–5114.
[14] C.M. Sung, M.F. Tai, Reactivities of transition metals with carbon: implications to the mechanism of diamond synthesis under high pressure, Int. J. Refract. Metals Hard Mater. 15 (1997) 237–256.
[15] X. Li, W. Cai, J. An, S. Kim, J. Nah, D. Yang, R. Piner, A. Velamakanni, I. Jung, E. Tutuc, S.K. Banerjee, L. Colombo, R.S. Ruoff, Large-area synthesis of high-quality and uniform graphene films on copper foils, Science 324 (2009) 1312–1314.
[16] O.S. Panwar, A.K. Kesarwani, S.R. Dhakate, B.S. Satyanarayana, Graphene synthesized using filtered cathodic vacuum arc technique and its applications, Vacuum 153 (2018) 262–266.
[17] Q. Zhou, L. Lin, Synthesis of graphene using micro chemical vapor deposition, in: in Proc. IEEE 23rd International Conference on Micro Electro Mechanical Systems (MEMS), Hong Kong, 2010, pp. 43–46, January 24–28.
[18] Q. Yu, J. Lian, S. Siriponglert, H. Li, Y.P. Chen, S.S. Pei, Graphene segregated on Ni surfaces and transferred to insulators, Appl. Phys. Lett. 93 (2008), 113103.
[19] M.G. Rybin, I.I. Kondrashov, A.S. Pozharov, V.C. Nguyen, N.M. Phan, E.D. Obraztsova, In situ control of CVD synthesis of graphene film on nickel foil, Phys. Status Solidi B 255 (2018), 1700414.
[20] Q. Hu, S.G. Kim, D.W. Shin, T.S. Kim, K.B. Nam, M.J. Kim, H.C. Chun, J.B. Yoo, Large-scale nanometer-thickness graphite films synthesized on polycrystalline Ni foils by two-stage chemical vapor deposition process, Carbon 113 (2017) 309–317.
[21] J.J. Lander, H.E. Kern, A.L. Beach, Solubility and diffusion coefficient of carbon in nickel: reaction rates of nickel-carbon alloys with barium oxide, J. Appl. Phys. 23 (1952) 1305–1309.
[22] L. Baraton, Z.B. He, C.S. Lee, C.S. Cojocaru, M. Châtelet, J.L. Maurice, Y.H. Lee, D. Pribat, On the mechanisms of precipitation of graphene on nickel thin films, EPL (Europhysics Letters) 96 (2011) 46003.
[23] L. Baraton, Z.B. He, C.S. Lee, J.L. Maurice, C.S. Cojocaru, Y.H. Lee, D. Pribat, in: L. Ottaviano, V. Morandi (Eds.), Study of Graphene Growth Mechanism on Nickel Thin Films, in GraphITA 2011, Springer, Berlin, 2012, pp. 1–7.
[24] A.C. Ferrari, J.C. Meyer, V. Scardaci, C. Casiraghi, M. Lazzeri, F. Mauri, S. Piscanec, D. Jiang, K.S. Novoselov, S. Roth, A.K. Geim, Raman spectrum of graphene and graphene layers, Phys. Rev. Lett. 97 (2006), 187401.
[25] Y.Y. Wang, Z.H. Ni, Z.X. Shena, Interference enhancement of Raman signal of graphene, Appl. Phys. Lett. 92 (2008), 043121.
[26] A. Dahal, M. Batzill, Graphene–nickel interfaces: a review, Nanoscale 6 (2014) 2548–2562.
[27] A. Di Bartolomeo, Graphene Schottky diodes: an experimental review of the rectifying graphene/semiconductor heterojunction, Phys. Rep. 606 (2016) 1–58.
[28] A. Cowen, R. Mahadevan, S. Johnson, B. Hardy, MetalMUMPs design handbook, MEMSCAP revision 4 (2012) 1–40.
[29] N.C. Craig, I.W. Levin, Calibrating Raman spectrometers with plasma lines from the argon ion laser, Appl. Spectrosc. 33 (1979) 475–476.
[30] P. Zeller, F. Speck, M. Weinl, M. Ostler, M. Schreck, T. Seyller, J. Wintterlin, Healing of graphene on single crystalline Ni(111) films, Appl. Phys. Lett. 105 (2014), 191612.
[31] E.K. Baumert, F. Sadeghi-Tohidi, E. Hosseinian, O.N. Pierron, Fatigue-induced thick oxide formation and its role on fatigue crack initiation in Ni thin films at low temperatures, Acta Mater. 67 (2014) 156–167.
[32] W.M. van Spengen, J.W.M. Frenken, The Leiden MEMS tribometer: real time dynamic friction loop measurements with an on-chip tribometer, Tribol. Lett. 28 (2007) 149–156.

Biographies

Alkisti Gkouzou received her BSc in Physics (2011) from the University of Patras and her MSc in microsystems and nanodevices (2013) from the National Technical University of Athens. She has been working as a PhD researcher at the Delft University of Technology. Her main interest focuses on evaluating nanoscale surface interactions, and improving the existing models that describe mechanisms during sliding motion of contacting surfaces. Highlights of her research include the reduction of capillary-induced adhesion in micro-electromechanical systems surfaces, and she also unraveled the dependence of dynamic friction on conformity and capillary kinetics. Currently, she is a design engineer at ASML Netherlands BV.

Prof. dr. Guido C.A.M. Janssen received both his MSc degree in Physics (1978) and his PhD (1983) from the University of Amsterdam. His MSc was in solid-state physics and the subject of his PhD was "Plasma heating by a Relativistic Electron Beam". His PhD work was carried out at the FOM institute for Atomic and Molecular Physics (AMOLF) in Amsterdam. During 1983 and1984 he worked for ASM, a Dutch semiconductor equipment company, on an Aluminum CVD process. In 1985 he joined Delft University of Technology, first as assistant professor and later as associate professor. His research topics at first were focused on semiconductor manufacturing, plasma-etching, chemical vapor deposition and sputter deposition. In 2000 his research interests shifted from thin films for semiconductor manufacturing to hard coatings. In 2006 he was appointed chair of Surfaces and Interfaces in the faculty Mechanical Maritime and Materials Engineering of TU Delft. With review papers on stress in thin films (2007, 2009) he concluded that line of research. Recently he started research into friction and wear, sponsored by NWO-I, the Dutch organization for fundamental research, as well as by m2i, a Dutch organization for applied research. His newest interest is in the deposition of graphene. His group at one time held the record for the largest flake of single-domain graphene (approximately 1 mm diameter) as well as for the highest mobility (75.000 $cm^2/V{\cdot}s$ at 4 K on BN, which is 1/3 of the mobility in exfoliated graphene).

Dr. ir. W. Merlijn van Spengen is an experienced analog electronics design expert, and the founding director of Falco Systems. He has worked at IMEC (Leuven), Leiden University and Delft University of Technology, in the fields of electronics, physics and mechanical engineering, specializing in instrumentation, MEMS reliability engineering and scanning probe microscopy. With his team at Falco Systems, Merlijn strives to provide the best laboratory amplifiers possible. He is also part-time associate professor in Delft, where he heads the MEMS reliability team supervising PhD researchers in the Precision and Microsystems Engineering department.